Research Article

Effects of high geotemperature and high altitude on the pressure wave of high-speed trains running in a long tunnel

Lei LIU, Lin JING[✉], Tian LI, Kaiyun WANG

State Key Laboratory of Rail Transit Vehicle System, Southwest Jiaotong University, Chengdu 610031, China

Abstract: Considering the high temperature distribution along a tunnel in a high-altitude area, the effects of high geotemperature and high altitude on the pressure wave of trains running in long tunnels were investigated using a three-dimensional, compressible, unsteady turbulence model. To reduce the simulation cost and reflect the pressure wave characteristics in long tunnels, a representative tunnel length was first determined for simulation. The simulation results indicated that compared to the condition of a normal ambient-temperature tunnel, when trains go through a high geotemperature tunnel, the distribution of the minimum pressure (P_{min}) along the tunnel moves to the tunnel entrance. The pressure amplitudes on the tunnel and train decrease integrally, with maximum reductions of 7.9% in the maximum pressure (P_{max}) and 44% in P_{min} on the tunnel, and 4.6% in P_{max} and 12% in P_{min} on the train. When trains meet in high geotemperature tunnels, the distributions of P_{max} and P_{min} along the tunnel change. The pressure amplitudes decrease integrally, with maximum reductions of 13.8% in P_{max} and 36.9% in P_{min} on the tunnel, and 7.1% in P_{max} and 15.6% in P_{min} on the train. The pressure difference between the two sides of the train during intersection decreases by 15.9%. As the altitude rises, when trains cross and meet in tunnels, the waveforms of pressures on the tunnel and train and the pressure difference between the two sides of the train remain unchanged, and the peaks decrease linearly.

Key words: High geotemperature; High altitude; High-speed train; Long tunnel; Pressure wave

1 Introduction

To satisfy the design requirements of high-speed railway lines, different kinds of structures are constructed along the track, such as tunnels, bridges, and embankments. With the increase in the speed of trains, the aerodynamic effect of the coupling system composed of the train, structure and airflow becomes more notable, and many aerodynamic problems appear or are exacerbated. Such problems include vehicle vibration under a crosswind (Liu et al., 2018; Chen et al., 2023), aerodynamic drag (Li et al., 2023; Zhang et al., 2021; Raghunathan et al., 2002; Baker, 2014) and air pressure waves in tunnels, which affect the ride comfort and cause damage to the car body structure and tunnel facilities (Niu et al., 2018a). With

[✉] Lin JING, jinglin@swjtu.edu.cn

[ORCID] Lin JING, https://orcid.org/0000-0003-2202-9683

the progress and development of high-speed railway technology, high-speed railways are being planned and constructed in some high-altitude areas with complex terrain and harsh natural environments, to promote the local economy. The section of the Sichuan-Tibet railway from Ya'an to Nyingchi under construction in China is one such railway. The average altitude of the line is about 3500 m and it has 69 tunnels with a total length of about 841.7 km, accounting for 82.6% of the total line. The longest tunnel reaches 42.4 km (Zhang et al., 2022). Therefore, the tunnel operation of trains in this section is frequent and the air pressure wave in tunnels is non-negligible. Due to dynamic geothermal activity, the temperature inside some tunnels reaches 60-80 °C (Zhao et al., 2023). The geological condition of the tunnel construction is shown in Fig. S1 (Zhao et al., 2023) in the Electronic Supplementary Materials. A geothermal source with a temperature of up to 850 °C below the line leads to complex geothermal activity, resulting in geological problems inside the tunnel, such as high geothermal temperature and water seepage. When trains run in long tunnels with

low atmospheric pressure and high temperature in high-altitude areas, the special environment affects the characteristics of aerodynamic pressure waves, thus affecting the normal operation of trains. Therefore, relevant studies on the effects of high geotemperature and high altitude on the pressure wave of high-speed trains are needed.

Through full-scale experiments, mobile model tests and numerical simulations, numerous scholars have studied the characteristics of air pressure waves of trains running in tunnels and the effect of key parameters of tunnels and trains in low-altitude areas with standard atmospheric pressure and normal temperature. Liu et al. (2017a) explored the effects of the tunnel length, train length and speed on the pressure wave in tunnels produced by the passage of high-speed trains through field tests. Liu et al. (2018) measured the air pressures to explore the pressure wave characteristics when trains go through tunnels. Gilbert et al. (2013a, 2013b) explored the aerodynamic pressure caused by a train traversing tunnels with different confining infrastructure using 1:25 scale mobile model tests. Using mobile model experiments, Miyachi et al. (2016) analyzed the pressure transient of trains with different nose shapes travelling through a tunnel. Zarnaghsh et al. (2019) conducted numerical simulations to investigate the alternating pressure and velocity fields when trains run in tunnels at different speeds. Liu et al. (2018) numerically studied the pressure wave characteristics when trains intersect in tunnels at the same and different speeds, and the dynamic response of the car body and side window to pressure waves were further explored (Jing et al., 2019). Li et al. (2019, 2021) conducted numerical simulations to explore pressure waves when high-speed trains go through a tunnel with an expanding portal and two adjoining and separated tunnels. Numerous studies have also been implemented to investigate the effects of the marshalling form (Niu et al., 2017), length (Niu et al., 2018a), nose shape (Li et al., 2017) and nose length (Chen et al., 2017) of a train on pressure waves resulting from trains running in tunnels.

Some researchers have also conducted exploratory studies on the air pressure waves when trains go through tunnels with low atmospheric pressure and high temperature in high-altitude areas, to investigate the influence of special environments on the aerodynamics of high-speed train/tunnel systems. Ling et al (2022) numerically investigated the effects of temperature and atmospheric pressure on the aerodynamic drag of trains passing through tunnels of the Sichuan-Tibet railway. The results showed that the aerodynamic drag increases as temperature decreases, and decreases as atmospheric pressure decreases. Luo (2016) and Huang et al. (2022) studied the effects of altitude on the pressure transient and passenger comfort when trains pass through tunnels using numerical simulations and found that the pressure peaks showed a linear decreasing trend with increasing altitude. Wang et al. (2021, 2022) conducted mobile model tests and numerical simulations to investigate the characteristics of pressure waves and micro-pressure waves produced by high-speed trains travelling through a tunnel with localized high temperature areas. The results indicated that the pressure gradient on the tunnel wall first decreases and then remains basically unchanged with the increase of the length and circumferential angle of the localized high temperature areas. Nevertheless, studies on the effect of high temperature on pressure waves have focused only on localized high temperatures in tunnels, the temperature was assumed to be constant, and a long tunnel length and low atmospheric pressure were not considered simultaneously. In this sense, considering the more realistic condition of the distribution of high temperature along an entire tunnel, the pressure wave characteristics inside a long tunnel in a high altitude area need to be further explored.

In this study, considering the distribution of high temperature along an entire tunnel, the pressure wave characteristics of high-speed trains passing through a tunnel and passing by each other in a long tunnel in a high-altitude area were numerically studied using a three-dimensional, compressible, unsteady turbulence model. The effect of the tunnel length was first analyzed to determine an appropriate tunnel length for simulations, to reduce the simulation cost and reflect the pressure wave characteristics of long tunnels. The effects of high temperature and high altitude on the pressure waves of high-speed trains going through and meeting in the tunnel were then investigated in detail.

2 Numerical simulation and algorithm verification

2.1 Train and tunnel models

Fig. 1 shows the full-scale model of the high-speed train. The three cars adopted in this study had a total length of 76.4 m, width of 3.38 m and height of 3.7 m. To reduce the calculation cost and ensure accuracy, the model retains the bogie and the streamlines of the nose and tail, but omits small features such as pantographs and other attachments. With reference to the design speed of high-speed trains on the Sichuan-Tibet Railway, a train speed of 200 km/h was selected in this study.
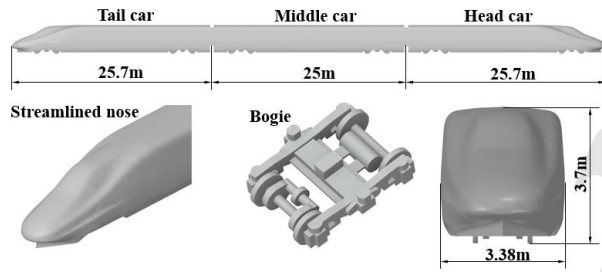

Fig. 1. Geometrical model of the high-speed train

The cross-section of the designed double-track tunnel of the Sichuan-Tibet Railway was selected for this study. The area of the cross-section is 81 m^2 and the distance between two lines is 4.5 m (Ling et al., 2022) (Fig. 2a). The line environment of the Layue tunnel was adopted. The elevation of the whole tunnel is about 2500 m, and the tunnel is affected by a high geothermal hazard. The predicted temperature along the Layue tunnel based on borehole temperature measurement data provided by the China Railway First Survey and Design Institute Group is shown in Fig. 2b (Zhang, 2021). The abscissa x/L_{tu} indicates the ratio of the distance between the location in the tunnel and the entrance to the tunnel length.

From an aerodynamic viewpoint, the most unfavorable tunnel length for trains passing through and intersecting in a tunnel can be calculated by the following equations (CEN, 2010):

$$L_{tu,crit} \approx \frac{L_{tr}}{4} \cdot \frac{c}{v} \cdot (1 + \frac{c}{v}) \tag{1}$$

$$L_{tu,crit} \approx \frac{cL_{tr}}{v} \tag{2}$$

where $L_{tu,crit}$ is the critical tunnel length; L_{tr} is the train length (76.4 m in this study); v is the train speed (55.55 m/s in this study); and c is the sound speed (m/s), which is affected by the temperature and can be calculated as follows:

$$c = 331.45 \times \sqrt{1 + T/273.15} \tag{3}$$

where T is the air temperature (°C).

According to Eqs. (1)-(3) and the temperature distribution in Fig. 2b, the most unfavorable tunnel length for trains passing and intersecting in the tunnel in this study are within the ranges of 820-960 m and 464-505 m, respectively. As these lengths are far less than the actual tunnel length, using them for simulation may not effectively reflect the characteristics of aerodynamic pressure waves in long tunnels. Meanwhile, the cost of using the actual length of the Layue tunnel (31 km) for simulation is high, and the aerodynamic pressure waves in the tunnel attenuate with increasing tunnel length. Therefore, an appropriate computational tunnel length between the actual length and the most unfavorable length was needed. Three tunnel lengths were selected for this study: 1 km, 3 km and 5 km. The temperature distribution along the tunnels of different lengths are shown in Fig. 2b.
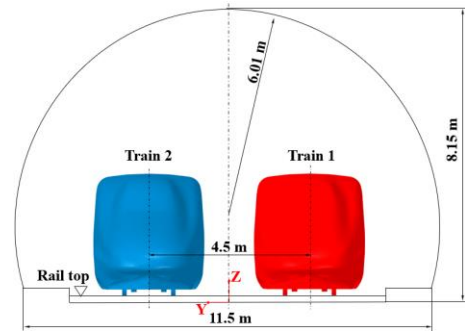
(a)
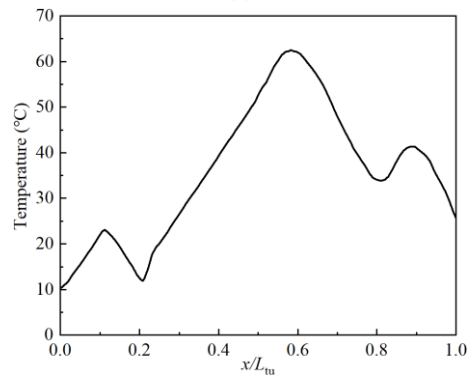
(b)

Fig. 2. Tunnel model and temperature distribution curve: (a) tunnel cross-section; (b) predicted temperature distribution along the Layue tunnel (Zhang, 2021)

2.2 Solver setting

As the air between the tunnel and train is restricted and compressed, the compressibility of the air cannot be ignored (Li et al., 2020). The airflow of trains going through and intersecting in a tunnel is unsteady and turbulent. Ji et al. (2019) and Wang et al. (2018) compared five commonly used turbulence models, namely realizable k-ε, RNG k-ε, standard k-ε, SST k-ω, and standard k-ω, for simulating pressure waves of trains running in tunnels. The results showed that the errors between the pressure calculated using different models and the results from moving model tests were almost within 10%., The RNG k-ε turbulence model, considered an effective and reliable turbulence model in the most recent studies (Xue et al., 2023; Li et al., 2022; Zhou et al., 2022; Zhang et al., 2018), has been widely used to simulate the pressure field induced by trains running in tunnels. The simulation results in these studies were in good agreement with experimental data. As a result, in this study we adopted a three-dimensional, compressible, unsteady RNG k-ε turbulence model in the software ANSYS FLUENT to simulate the pressure wave in tunnels. The y+ on the train surface is about 300, which satisfies the usage conditions of the wall function (Niu et al., 2018a), and the standard wall function was used to bridge the wall-affected region and the fully turbulent region (Niu et al., 2018a; Chu et al., 2014). The SIMPLE algorithm was used to realize pressure-velocity coupling (Wang et al., 2021, 2022). The time step was set to 0.005 s (Li et al., 2021; Liu et al., 2017b). Based on the time step, minimum grid size of the tunnel surface, and propagation speed of pressure waves, the estimated Courant number was about 9, close to those of Niu et al. (2018b) and Yang et al. (2019). The second-order implicit scheme was applied in the time discretization process in the model (Niu et al., 2018a; Chu et al., 2014).

2.3 Computational region and boundary conditions

Fig. 3 shows the computational region and boundary conditions of trains going through and intersecting in a tunnel. The entire region consists of a sliding region including the train, and a static region including the open area outside the tunnel and the gap between the sliding region and the tunnel wall. The open area outside the tunnel consists of two cuboids 300 m long, 120 m wide and 60 m high (Wang et al., 2022), to ensure that the flow near the tunnel portals is not affected by the outer domain. The sliding mesh method was used between the two regions through the interface to implement the data exchange and relative sliding of regions. The train surface, tunnel wall, ground and front of the open area were set as the no-slip wall, and other boundaries of the open area were set as the pressure outlet. The train was placed 50 m from the tunnel portals to avoid the pressure fluctuation when trains enter the tunnel (Liu et al., 2017b). The operating pressure of the entire region was set to the values corresponding to the altitude, to simulate the condition of the realistic atmospheric pressure of different altitudes. To realize the high temperature inside the tunnel, before the train entered, the air temperature of the entire region was set to the normal ambient temperature corresponding to the altitude, and when the train was about to enter, the tunnel wall was set as the constant temperature boundary according to the temperature distribution in Fig. 2b. The air temperature inside the tunnel was set to the value corresponding to the wall of different longitudinal positions, through patch initialization.
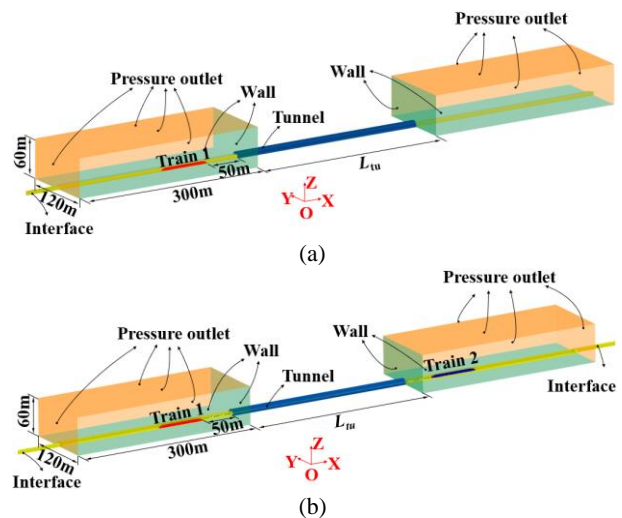

(a)

(b)

Fig. 3. Computational region and boundary conditions: (a) a train passing through the tunnel; (b) two trains passing by each other in the tunnel.

2.4 Grid scheme

The hybrid grid scheme is shown in Fig. 4. Due to the complexity of the train structure, the tetrahedral shape was adopted for the grid of the sliding region close to the train, while the prism was adopted for the region away from the train. The hexahedral grid was implemented in the static region as it has a geometrically regular shape. The surface grids of the head car and tunnel portal are shown in Figs. 4b and 4c. The surface mesh of the streamline parts of train were locally densified due to its complex geometry.
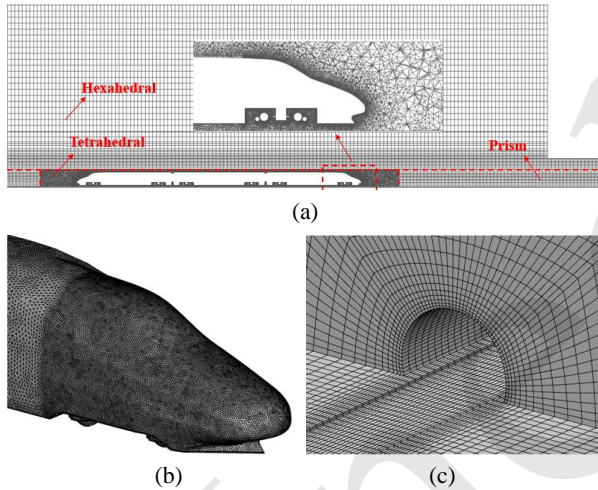

Fig. 4. Grid diagram: (a) longitudinal section of the computational region; (b) surface mesh of the head car; (c) surface mesh at the tunnel portal

To verify the grid independence, three grid generation schemes were conducted for calculation. Trains going through a 500-m tunnel (Section 2.6) was selected as the validation case. The minimum grid sizes and total numbers of grids of three schemes are shown in Table S1 in the Electronic Supplementary Materials. The pressure variation curves of observation points on the tunnel wall and train surface calculated using the different grid schemes are shown in Fig. S2 in the Electronic Supplementary Materials. The deviations of pressure peak values of points on the tunnel wall and train surface calculated using the coarse grid scheme and middle grid scheme were 0.95% and 1.46%, respectively, and those calculated using the middle grid scheme and fine grid scheme

were 0.78% and 0.46%, respectively. As a result, to reduce the amount of calculation, the middle grid scheme was adopted in this paper. The total numbers of grids of models of the train passing through the 1-km, 3-km and 5-km tunnels were 8 million, 10 million and 12 million, respectively, and those of models of two trains passing by each other were 10.3 million, 12.5 million and 14.8 million, respectively.

2.5 Observation point layout

The layout of pressure observation points on the train and tunnel is shown in Fig. 5. The points TR_1 and TR_11 were located at the tips of the nose and tail, respectively. There were 49 pressure observation points on the tunnel, which were 1 m above the rail top. The spacing between each point was $0.02L_{tu}$, to compare the cases under different tunnel lengths conveniently. For cases of the passage of a train, the pressure observation points on the tunnel and train were located at the narrower side, as the changes on that side are more obvious than those on the wider side (Li et al., 2019). For cases of two trains intersecting, the pressure observation points on the tunnel were located on the narrower side, and those on the train were located on both sides. The points TR_2a to TR_10a were located on the side near the tunnel, and points TR_2b to TR_10b on the other side.
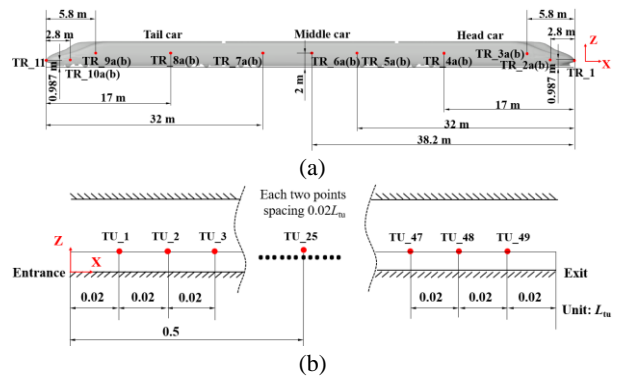

Fig. 5. Layout of the observation points: (a) on the train surface; (b) on the tunnel wall

2.6 Verification of the algorithm

The precision of the numerical algorithm in this study was verified through comparison with the results of Liu et al. (2017b). The validation cases were trains travelling through and intersecting in the tunnel at the speed of 350 km/h, with a tunnel length of 500

m and a cross-sectional area of 100 m^2. The results are shown in Figs. S3 and S4 in the Electronic Supplementary Materials. The pressure observation point on the tunnel was 6 m from the tunnel portal and 1 m above the rail top, and that on the train was located at the same level as the train nose tip and 2.845 m from it. The pressure waveforms of the present results and those of Liu et al. (2017b) fit well. The deviations of the pressure peak-peak values of observation points on the tunnel and train are 1.4% and 6.6%, respectively, when trains travel through the tunnel, and 2.1% and 9.2%, respectively, when trains intersect in the tunnel. Therefore, the present numerical algorithm is accurate and reliable.

3 Determination of the computational tunnel length

3.1 Computational tunnel length for the train passing through the tunnel

3.1.1 Pressure wave characteristics in the tunnel

The case of a train travelling through the 1-km tunnel was taken as an example to analyze the pressure wave characteristics. The propagation processes of pressure waves and the pressure variation of observation points on the tunnel and train are depicted in Fig. S5 in the Electronic Supplementary Materials. In Fig. S5a, the Y-axis denotes the distance from the tunnel portal and the black lines denote the locations of the tips of the train nose and tail. The colored full and broken lines respectively denote compression waves and expansion waves travelling at the speed of sound, which are provoked by the entry of the train nose and tail, respectively. When they reach the tunnel exit, most of them reflect as pressure waves of the contrary nature. The arrival of the compression wave and expansion wave causes the pressures on the tunnel and train to rise and drop, respectively. In Figs. S5b and S5c, the vertical colored full and broken lines respectively represent the arrivals of compression waves and expansion waves, and the grey area represents the train-passage. At 0 s, the train enters the tunnel and compresses the air in front of it (called the "piston effect"), inducing the pressure of the train nose tip (TR_1) to rise sharply and provoking a compression wave to propagate forward. When it reaches the tunnel midpoint (TU_25), the pressure rises rapidly. With the further entry of the

train, the pressures of TR_1 and TU_25 have a slight second rise due to the friction effect of air, and then drop as the expansion wave arrives. In addition, as the train moves away the air around it forms a high pressure region in front of it and a negative pressure region on each side of it. When it passes observation points on the tunnel, the pressure first rises slightly, then drops rapidly, and recovers after the train passes completely.

3.1.2 Determination of tunnel length

The propagation process of pressure waves and the corresponding pressure variation curves of TU_25 and TR_1 during the passage of trains through the tunnels with lengths of 3 km and 5 km are depicted in Figs. S6 and S7 in the Electronic Supplementary Materials, respectively. Δt_1 and Δt_2 indicate the time interval between the compression waves and expansion waves arriving at TU_25 and TR_1, respectively. Δt_3 and Δt_4 indicate the time interval between two adjacent expansion waves arriving at TU_25 and TR_1, respectively. They can be calculated as follows:

$$\Delta t_1 = \frac{L_{tr}}{v} \tag{4}$$

$$\Delta t_2 = \frac{cL_{tr}}{v(c+v)} \tag{5}$$

$$\Delta t_3 = \frac{L_{tu}}{c} - \frac{L_{tr}}{v} \tag{6}$$

$$\Delta t_4 = \frac{2L_{tu}}{c+v} - \frac{cL_{tr}}{v(c-v)} \tag{7}$$

According to Eqs. (4) and (5), Δt_1 and Δt_2 are independent of the tunnel length, indicating the time lengths for the pressures of TU_25 and TR_1 to reach the positive peaks caused by rise-drop or the negative peaks caused by drop-rise remain unchanged, and only the peaks decrease slightly due to the stronger attenuation of pressure waves in longer tunnels. Within the time interval between two adjacent expansion waves or two adjacent compression waves arriving at the observation point, the pressures at TU_25 and TR_1 have a relatively long and stable stage, such as Δt_3 and Δt_4, which increases as the tunnel length increases according to Eqs. (6) and (7).

As a result, the stable stage is prolonged accordingly, while the pressure values remain basically unchanged. The subsequent stable stages also show the same situation. However, in the 1-km tunnel, stable pressure stages are too short to be clearly distinguishable. With the tunnel length increasing from 3 km to 5 km and much longer lengths, only the pressure waveforms have a great effect on the time length of the stable pressure stages.

The distributions of the maximum pressure (P_{max}) and minimum pressure (P_{min}) along the tunnel when a train passes through the 1-km, 3-km and 5-km tunnels, are presented in Figs. S8a and S8b in the Electronic Supplementary Materials. The P_{max} is induced first by the arrival of the compression wave and the friction effect, and decreases as the distance from the observation points to the tunnel portal increases due to attenuation of the compression wave. However, when the distance is less than the train length, as the P_{max} is also affected by the train's passage, it first increases and then decreases. When the distance is more than x_1 (Figs. S5a and S6, Electronic Supplementary Materials), as the reflected expansion wave arrives earlier, the pressure drops in advance, causing the P_{max} to decrease faster. The x_1/L_{tu} is expressed as follows:

$$x_1 / L_{tu} \approx 1 - \frac{cL_{tr}}{2vL_{tu}} \tag{8}$$

where c is set to 352 m/s, which is the median number within the range (337-367 m/s) calculated according to the temperature in Fig. 2b and Eq. (3) in the text.

Under different tunnel lengths, except at observation points closer to the tunnel portal and exit, the distribution of P_{max} remains basically unchanged, and in longer tunnels, the values decrease due to the stronger attenuation of the compression wave. Eq. (8) shows that when L_{tu} increases from 1 km to 3 km, x_1/L_{tu} increases from 0.76 to 0.92, representing a change relative to the entire tunnel of 16%, and when the L_{tu} further increases to 5 km, the x_1/L_{tu} increases to 0.94, representing a change relative to the entire tunnel of 2%. Furthermore, the x_1/L_{tu} increases as the tunnel length increases and is always less than 1. Therefore, with L_{tu} increasing from 3 km to 5 km and much longer lengths, the change of x_1/L_{tu} relative to

the entire tunnel is always less than 8%. P_{min} results from the expansion wave and the train's passage. As presented in Figs. S5b and S7a (Electronic Supplementary Materials), the expansion wave reaches TU_25 during the passage of the train in the 1-km tunnel. Their superposition effect enhances the P_{min} of TU_25, resulting in a value 35.7% higher than that in the 3-km tunnel. The expansion wave does not reach TU_25 during the train's passage in the 3-km and 5-km tunnels. In the 5-km tunnel, the value of P_{min} decreases by only 0.9% and the gap between the arrival of the expansion wave and passage of the train increases, indicating that with the tunnel length increasing from 3 km to 5 km and much longer lengths the two will not coincide. At other observation point locations, the chances of the expansion wave encountering the train's passage are similar, thus the distribution of the P_{min} along the tunnel length is roughly consistent.

Figs. S8c and S8d (Electronic Supplementary Materials) show the distributions of P_{max} and P_{min} along the train, and x/L_{tr} indicates the ratio of the longitudinal distance from observation points on the train to the train nose tip to the train length. Under different tunnel lengths, the distributions of P_{max} and P_{min} remain unchanged. As the tunnel length increases, the P_{max} of observation points on the nose and constant section body of the train basically remain unchanged, as they result from the piston effect and friction effect, while those on the train tail decrease, as they result from the compression wave, and the values of P_{min} decrease as they result from the expansion wave.

To sum up, under different tunnel lengths, the distributions of P_{max} and P_{min} along the train remain basically unchanged. With tunnel length increasing from 1 km to 3 km, the waveforms of pressures on the tunnel and train and the distributions of P_{max} and P_{min} along the tunnel change greatly, but with the tunnel length increasing from 3 km to 5 km and much longer lengths, the pressure waveforms change only in the duration of the stable pressure stage, and the distribution of P_{max} and P_{min} remains roughly unchanged. Although with increasing tunnel length, reductions of P_{max} and P_{min} on the tunnel and train are inevitable due to the attenuation of pressure waves, based on the above results, the characteristics of pressures on the

tunnel and train in the 3-km tunnel can effectively reflect those in longer tunnels. Therefore, 3 km was determined as an appropriate computational tunnel length for a train passing through tunnels.

3.2 Computational tunnel length for two trains passing by each other in a tunnel

3.2.1 Pressure wave characteristics in the tunnel

The case of trains meeting in a 1-km tunnel was taken as an example to analyze the pressure wave characteristics. Fig. S9 (Electronic Supplementary Materials) shows the propagation processes of pressure waves in the tunnel and the pressure variation curves of observation points on the tunnel and train. As the temperature along the tunnel is distributed asymmetrically about the tunnel midpoint, the speed of pressure waves from the tunnel portal and exit are different. Consequently, the moments when they reach TU_25 have a small interval.

3.2.2 Determination of tunnel length

The propagation processes of pressure waves and the pressure variation curves at TU_25 and TR_1 in the 3-km and 5-km tunnels are shown in Figs. S10 and S11 (Electronic Supplementary Materials). $\Delta t'_1$-$\Delta t'_4$ can be calculated as follows:

$$\Delta t'_1 = \frac{L_{tr}}{v} \tag{9}$$

$$\Delta t'_2 = \frac{cL_{tr}}{v(c+v)} \tag{10}$$

$$\Delta t'_3 = \frac{L_{tu}}{c} - \frac{L_{tr}}{v} \tag{11}$$

$$\Delta t'_4 = \frac{L_{tu}}{c+v} - \frac{cL_{tr}}{v(c-v)} \tag{12}$$

where the small time interval between the pressure waves from the tunnel portal and exit reaching TU_25 is ignored in Eqs. (9) and (11).

Similar to cases of trains travelling through tunnels of different lengths, according to Eqs. (9)-(12), the tunnel length affects only $\Delta t'_3$ and $\Delta t'_4$, which indicates that the times for the pressures at TU_25 and TR_1 to peak remain unchanged. The

pressure waveforms have a big effect only on the duration of the stable stages with tunnel length increasing from 3 km to 5 km and much longer lengths.

Fig. S12(a) (Electronic Supplementary Materials) shows the distribution of P_{max} along the tunnel when two trains pass each other in the 1-km, 3-km and 5-km tunnels. The overall distribution is roughly symmetrical about the tunnel midpoint, with a high in the middle and a low at each end. The P_{max} results from the first arrivals of the compression wave provoked by the entry of the noses of train 1 (C1) and train 2 (C2). The closer the distance between the observation points and the tunnel midpoint, the shorter the time interval between the first arrivals of C1 and C2. Thus, their superposition effect is stronger, which enhances the P_{max}. At the position where x/L_{tu} is 0.16, the P_{max} increases sharply due to the superposition effect of the first arrival of C2 and the high pressure region in front of train 1, as shown by the point x_2 in Figs. S9 and S10 (Electronic Supplementary Materials). x_2/L_{tu} can be calculated as follows:

$$x_2 / L_{tu} \approx \frac{v}{c+v} \tag{13}$$

Eq. (13) shows that x_2/L_{tu} is independent of the tunnel length. Therefore, under different tunnel lengths, the point at which the P_{max} increases sharply is roughly the same. At the point where x/L_{tu} is 0.84, although the superposition of the first arrival of C1 and the high pressure region in front of train 2 occurs, the area between the observation point and train 2 is wide, the pressure is less affected by the high pressure region, and a sharp increase of P_{max} is not obvious. After the distance from observation points to the tunnel portal is more than x_3 (Figs. S9a and S10, Electronic Supplementary Materials), as the first arrival of C2 is earlier than the first arrival of the expansion wave provoked by the entry of the tail of train 1 (E1), the superposition effect of the first arrivals of C1 and C2 is no longer weakened by E1. Thus, P_{max} increases faster. x_3/L_{tu} can be calculated as follows:

$$x_3 / L_{tu} \approx 0.5 - \frac{cL_{tr}}{2vL_{tu}} \tag{14}$$

According to the Eq. (14), when the tunnel length is 1 km, 3 km or 5 km, the values of x_3/L_{tu} are 0.26, 0.42

and 0.45 respectively, which are roughly the same as those at the position where the P_{max} starts to rise faster in Fig. S12a (Electronic Supplementary Materials). With the tunnel length increasing from 1 km to 3 km, the change of x_3/L_{tu} relative to the entire tunnel is 16%, reducing to 3% as the tunnel length increases to 5 km. Furthermore, x_3/L_{tu} increases as the tunnel length increases and is always less than 0.5. Therefore, with the tunnel length increasing from 3 km to 5 km and much longer lengths, the change of x_3/L_{tu} relative to the entire tunnel is less than 8%.

The distribution of the P_{min} values along the tunnel is shown in Fig. S12b (Electronic Supplementary Materials). They also distribute roughly symmetrically about the tunnel midpoint. With the tunnel length increasing from 1 km to 3 km, the situation whether the expansion wave encounters the train-passage changes, resulting in changes in the distribution and values of P_{min}. However, with the tunnel length increasing from 3 km to 5 km and much longer lengths, the likelihood of the expansion wave encountering the passing train remains almost unchanged, thus the changes in the distribution and values of P_{min} are small. Unlike the case of trains going through tunnels (Fig. S11b, Electronic Supplementary Materials), the P_{max} at TR_1 occurs at the second peak, as it results from the first arrival of C2. Simultaneously, the P_{min} at TR_1 occurs as the trains intersect, as it is affected by the pressure drop caused by the passage of train 2. As depicted in Figs. S12c and S12d (Electronic Supplementary Materials), under different tunnel lengths, the distributions of P_{max} and P_{min} along the train are the same but the values decrease due to the more severe attenuation of pressure waves in longer tunnels.

Similar to the determination of the tunnel length for the passage of trains, based on the above analysis, the characteristics of pressures on the tunnel and train when two trains meet in a 3-km tunnel can effectively reflect those in longer tunnels. Therefore, 3 km was also selected as the computational tunnel length for two trains passing each other in a tunnel.

4 Simulation results and discussion

4.1 Effect of high geotemperature on the pressure wave

The effect of high geotemperature on pressure waves was investigated by comparing the cases of trains passing through and intersecting in the tunnel at high temperature and normal ambient temperature. The distribution of high temperature along the tunnel is shown in Fig. 2b, with a maximum temperature (T_{max}) of 62.5 °C. The normal ambient temperature (T_N) corresponding to the altitude of 2500 m is −1.25 °C.

4.1.1 Trains passing through tunnels

Fig. 6 shows the distributions of P_{max} and P_{min} along the tunnel for trains passing through the ambient-temperature and high-temperature tunnels. The distributions of P_{max} along the tunnel at the two temperatures are the same. The P_{max} at high temperature is smaller than that at ambient temperature, with a maximum reduction of 7.9%. When the train enters the ambient-temperature and high-temperature tunnels, the air temperature and air density around the tunnel portal are as depicted in Fig. 7. The distribution of the air density is roughly the same as that of the air temperature. The air density decreases as the temperature rises, which reduces the compression wave, thereby reducing the P_{max}. The distribution and values of P_{min} along the tunnel at high temperature both change. Compared to the case at ambient temperature, the maximum reduction of the P_{min} reaches 44% at TU_19, and the maximum increase reaches 89.5% at TU_41. The difference in the P_{min} at the two temperatures is much greater than that in the P_{max}.
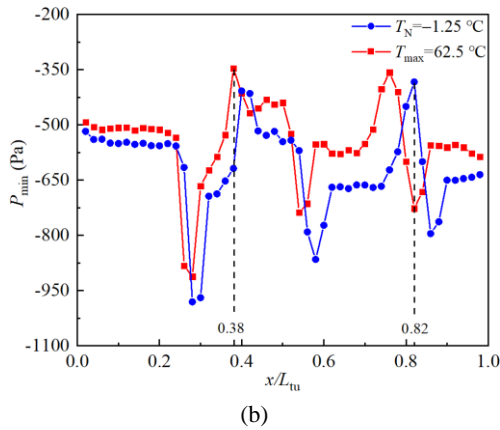

(a)

(b)
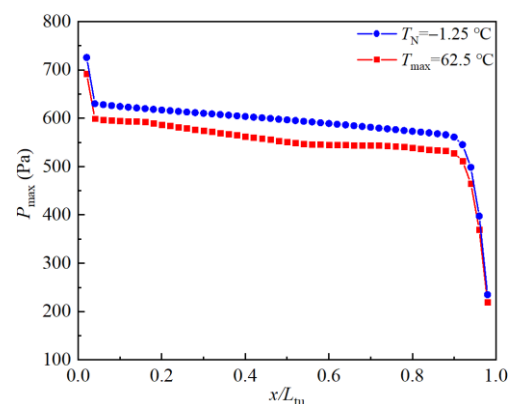
Fig. 6. Distributions of P_{max} and P_{min} along the tunnel when trains pass through an ambient-temperature tunnel and high-temperature tunnel: (a) P_{max}; (b) P_{min}. T_N indicates that the temperature inside the tunnel is the normal ambient temperature outside the tunnel. T_{max} denotes the maximum temperature inside the high geotemperature tunnel
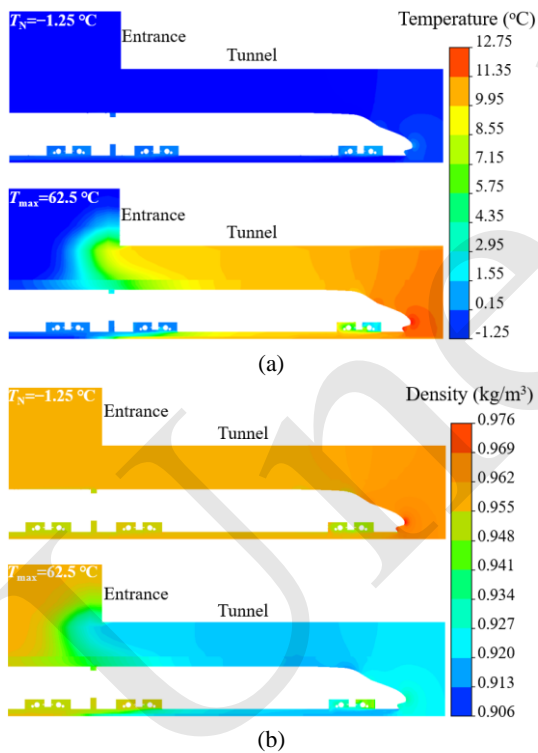

(a)

(b)

Fig. 7. Airflow field distributions of trains entering the ambient-temperature and high-temperature tunnels: (a) temperature fields in the ambient-temperature tunnel and high-temperature tunnel, respectively; (b) air density fields in the ambient-temperature tunnel and high-temperature tunnel, respectively

Fig. 8 shows the pressure variation curves at TU_19 and TU_41, where x/L_{tu} is 0.38 and 0.82, respectively. Fig. 9 shows the propagation process of pressure waves when trains pass through tunnels at different temperatures. The speed of propagation of pressure waves increases as the temperature rises. This affects the superposition of the train-passage and pressure waves, thereby affecting the P_{min} along the tunnel. At ambient temperature, the compression wave arrives at TU_19 after the pressure drop induced by the passing train. At high temperature, it arrives in advance, before the passage of the train. This balances part of the pressure drop, resulting in the value of the P_{min} being 44% smaller than that at ambient temperature. At ambient temperature, the compression wave reaches TU_41 before passage of the train, which balances part of the pressure drop, and the expansion wave arrives after the pressure recovers. At high temperature, they arrive in advance and both before passage of the train. Thus, the pressure drop is not affected by them, resulting in the value of the P_{min} being 89.5% bigger than that at ambient temperature.

In addition, as shown in Fig. 6, the peaks of the P_{min} along the tunnel at high temperature move to the tunnel portal. The distance between the peaks of the P_{min} at the two temperatures increases as the distance from observation points to the tunnel portal increases. The first peaks of the P_{min} both appear at the position where x/L_{tu} is 0.28. The last one at ambient temperature appears at the position where x/L_{tu} is 0.82 and the last one at high temperature appears at the position where x/L_{tu} is 0.86. The pressure peaks on the tunnel at high temperature appear increasingly earlier than those at ambient temperature, such as at TU_19 (Figs. 8 and 9). The time interval between the first pressure peaks at the two temperatures is 0.13 s, while the time between the final pressure peaks is 3.04 s. The above phenomena result from the faster propagation of pressure waves at high temperature, and as pressure waves continuously reflect and propagate, the distance difference between pressure waves at the two temperatures increases.
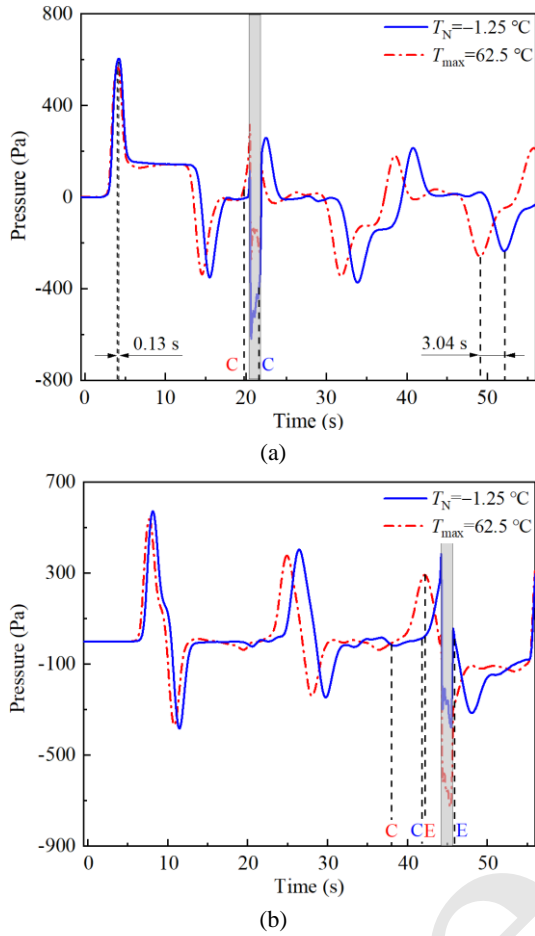
Fig. 8. Curves of pressure variation at observation points on the tunnel when trains pass through the ambient-temperature tunnel and high-temperature tunnel: (a) TU_19; (b) TU_41
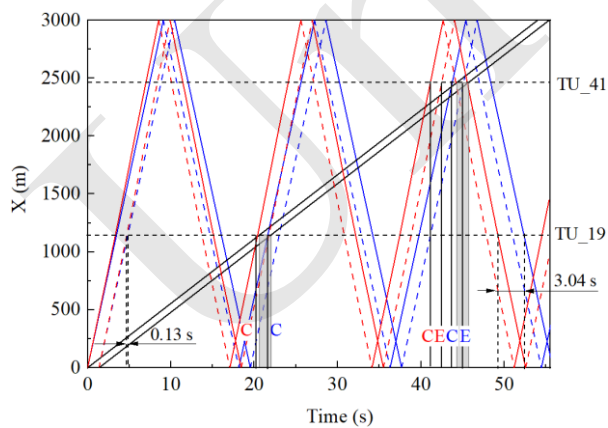

Fig. 9. The propagation process of pressure waves when trains pass through tunnels at different temperatures. The blue and red respectively denote pressure waves at ambient temperature and high temperature, and full and broken lines respectively denote compression waves and expansion waves

Fig. 10 shows that the distributions of P_{max} and

P_{min} along the train at the two temperatures are the same, and the P_{max} values at high temperature are smaller than those at ambient temperature. In the high-temperature tunnel, the air density is lower, reducing the piston and friction effects, and as those at TR_1 are the strongest, the difference of the P_{max} at TR_1 is the most apparent, with a 4.6% reduction. The pressure variation curve of TR_1 is shown in Fig. 11. ΔP_1 and ΔP_2 represent the pressure rise resulting from the piston effect and the friction effect, respectively. They decrease by 65 Pa and 29 Pa at high temperature, respectively, compared to those at ambient temperature. Although the ΔP_2 at high temperature decreases, the friction effect is not only reduced with the air density decreasing, but also enhanced with the air viscosity increasing. The reduction of ΔP_2 indicates that the change of the friction effect with the air density is greater than that with the air viscosity with the temperature rising. At high temperature, except when the P_{min} of TR_1 is 12% lower than that at ambient temperature, the P_{min} values of the observation points are about 6% higher. Although the decrease of the air density reduces the expansion wave, for TR_1, the reduction effect of the temperature rise on the piston effect and friction effect is greater than that on the expansion wave, causing a reduction of the pressure rise larger than that of the pressure drop. In addition, the pressure peaks on the train at high temperature also gradually appear earlier, and the time interval between the first pressure peaks of TR_1 resulting from pressure waves at the two temperatures is 0.83 s, while that between the final pressure peaks is 2.39 s.
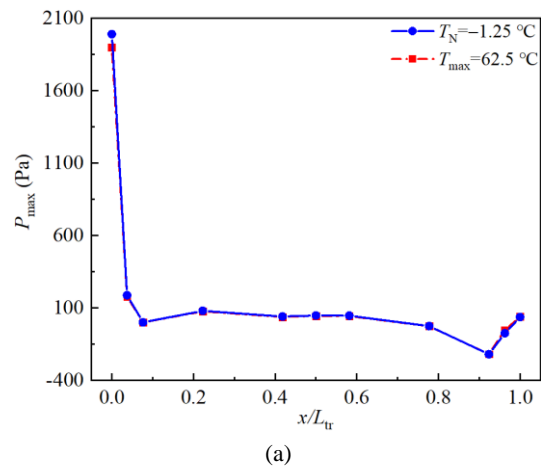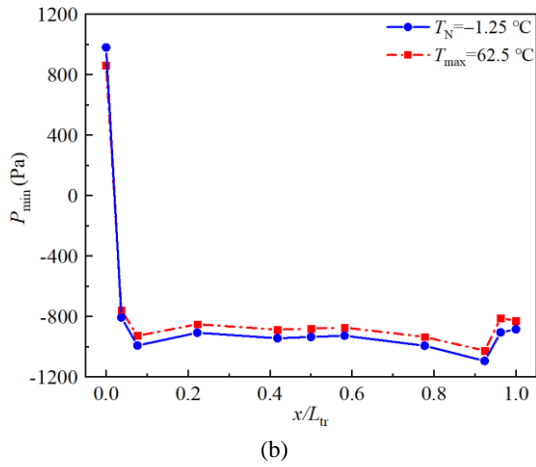

(a)

(b)

Fig. 10. Distributions of P_{max} and P_{min} along the train when it passes through the ambient-temperature tunnel and high-temperature tunnel: (a) P_{max}; (b) P_{min}
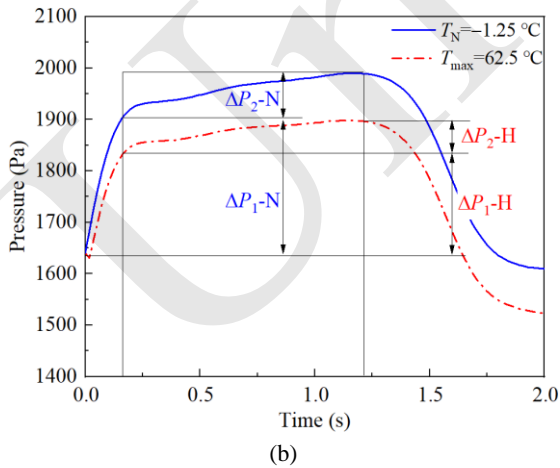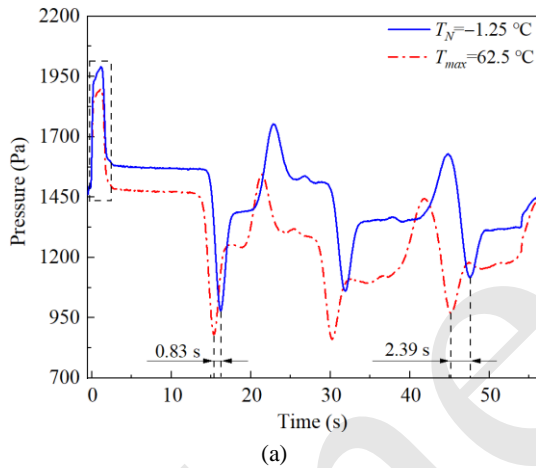

(a)

(b)

Fig. 11. Curves of pressure variation at observation points on the train when trains pass through the ambient-temperature tunnel and high-temperature tunnel. The plot on the right is an enlargement of the dashed rectangle in the plot on the left

4.1.2 Two trains passing by each other in a tunnel

Fig. 12 shows the distributions of P_{max} and P_{min} along the tunnel for two trains meeting in the ambient-temperature and high-temperature tunnels. The P_{max} at TU_25 is the largest at the two temperatures. The P_{max} values at high temperature are generally lower than those at ambient temperature: the decrease in P_{max} is 7.5% at TU_25 and 13.8% (the largest reduction) at TU_8. Fig. 13 shows the pressure variation curves of TU_8 and TU_25. At high temperature, the decrease of the air density reduces compression waves. At TU_8, as the second pressure peak at ambient temperature appears later than that at high temperature and encounters the high pressure region in front of train 1, their superposition enlarges the difference of P_{max}. In addition, the symmetrical point of the distribution of P_{max} along the tunnel at high temperature moves slightly toward the tunnel portal. As shown in Fig. 2b, the temperature from the tunnel midpoint to the tunnel exit is higher than that from the tunnel midpoint to the tunnel portal. Fig. 14 shows the propagation process of pressure waves when trains pass through tunnels at different temperatures. The C2 wave propagates faster than C1, causing their point of intersection to move to the tunnel portal. The time interval between the first arrivals of C1 and C2 at the observation point on the left side of the tunnel midpoint is shorter than that on the right side, thus the superposition effect is stronger, resulting in the P_{max} on the left side being bigger than those on the right symmetrical position. Compared to the case at ambient temperature, at high temperature, the maximum increase of the P_{min} reaches 42.5% at TU_13, and the maximum reduction of the P_{min} reaches 36.9% at TU_39. The distribution of the P_{min} changes, as the change of the propagation speed of pressure waves affects their superposition and the train-passage. As the temperatures at both sides of the tunnel midpoint are the same at ambient temperature, the symmetry of the distribution of the P_{min} about the tunnel midpoint is stronger than that at high temperature.
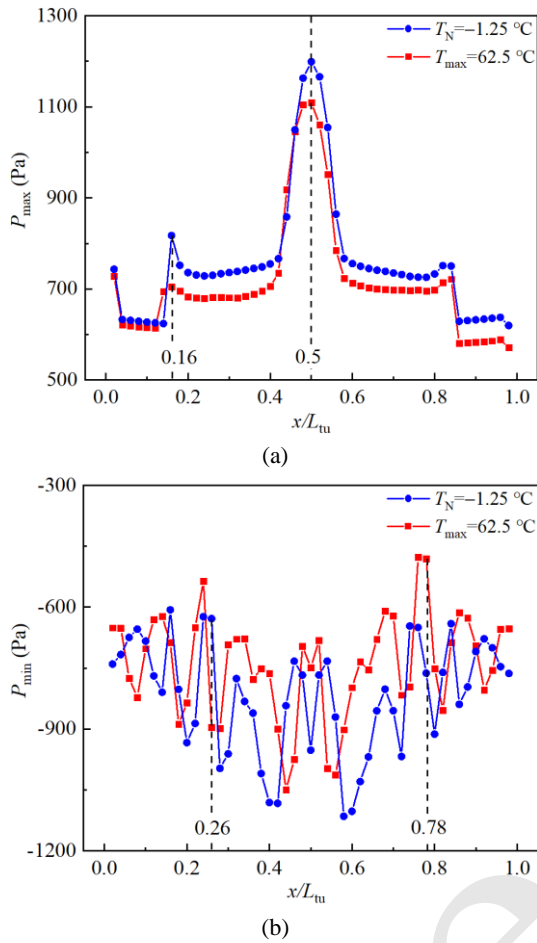
(a)

(b)

Fig. 12. Distributions of P_{max} and P_{min} along the tunnel when two trains pass each other in the ambient-temperature tunnel and high-temperature tunnel: (a) P_{max}; (b) P_{min}
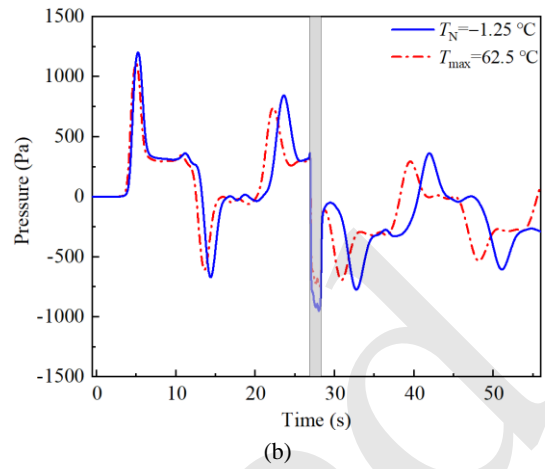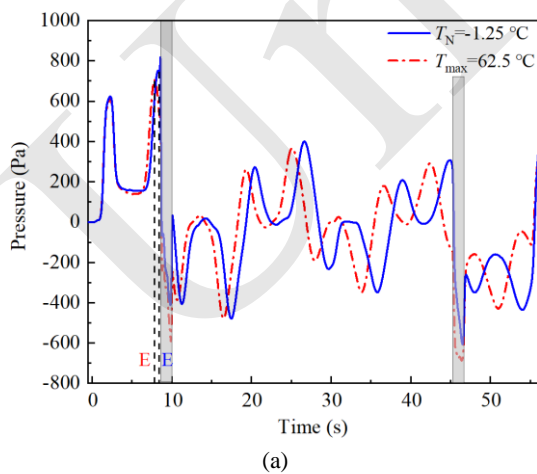

(a)

(b)

Fig. 13. Curves of pressure variation at observation points on the tunnel when two trains pass each other in the ambient-temperature tunnel and high-temperature tunnel: (a) TU_8; (b) TU_25
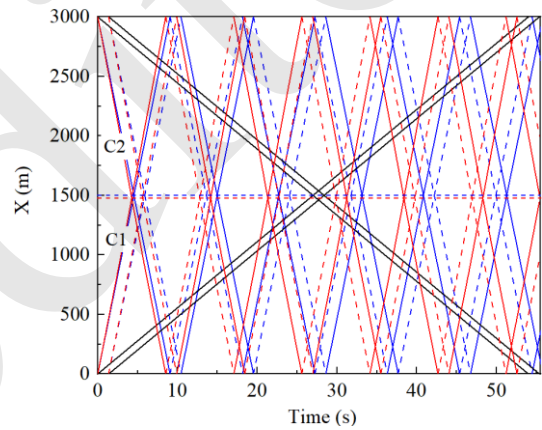

Fig. 14. The propagation process of pressure waves when trains pass through tunnels at different temperatures. The red and blue horizontal lines respectively represent the locations where C1 encounters C2 when trains meet in tunnels at different temperatures

Fig. S13 (Electronic Supplementary Materials) shows the distributions of P_{max} and P_{min} along the two sides of the train at ambient temperature and high temperature. The distributions at the two temperatures are roughly the same. The P_{max} values at high temperature are smaller than those at ambient temperature as the P_{max} results not only from the piston and friction effects, but also the first arrival of C2, and the P_{min} results from the expansion wave and train 2 passing (Fig. S14, Electronic Supplementary Materials). Compared to the case at ambient temperature, at high temperature, as the air density is lower, the compression wave is reduced, causing the P_{max} to decrease, and the change at TR_1 is the most

apparent, with a 7.1% reduction. The expansion wave and the pressure drop induced by the passing train are also reduced, causing the P_{min} to decrease. The difference at TR_3b is the most apparent, with a 15.6% reduction.

Fig. S15 (Electronic Supplementary Materials) depicts the variation curve of the pressure difference between two observation points, one on each side of the middle car (the pressure difference between TR_6a and TR_6b. The pressure difference fluctuates slightly when the train enters and leaves: there are two slight fluctuations when the windshield of train 2 passes and two large fluctuations when the trains intersect, as the pressure of the observation point on the side of train 1 close to train 2 is more affected by the high pressure region and negative pressure region around train 2. When the nose of train 2 nose passes, the pressure difference shows first a negative and then a positive fluctuation, while when the tail of train 2 passes, it shows first a positive and then a negative fluctuation. At high temperature, the decrease of the air density reduces the pressure of the region around the train, causing the peak-peak value of the pressure difference during intersection to decrease by 15.9%.

4.2 Effect of high altitude on pressure wave

4.2.1 Trains passing through tunnels

Fig. 15 shows the pressure variation curves of TR_25 and TR_1 for trains travelling through the high-temperature tunnels at different altitudes. In this study, the temperature inside the tunnel was assumed to result mainly from the high geothermal environment inside the tunnel. The influence of temperature changes outside the tunnel caused by changes in altitude on the temperature inside the tunnel was assumed to be negligible. Thus, as the altitude rises, the temperature inside the tunnel does not change, and the propagation speed of pressure waves in the tunnel remains unchanged. Thus, their superposition and the train's passage are not affected, and the distributions of P_{max} and P_{min} along the tunnel and train also remain unchanged. Therefore, they are not explored further in this Section. The pressure waveforms of TR_25 and TR_1 remain unchanged, and the pressure peaks decrease with the rise in the altitude, as the air density decreases with the rise in the altitude, reducing the pressure waves, piston

effect, friction effect and the pressure drop resulting from the train's passage. The fitted curves and equations between the P_{max} and P_{min} of TR_25 and TR_1 and the altitude are shown in Fig. 16. The P_{max} and P_{min} decrease linearly with the rise in the altitude, and the fitted R^2 coefficients are more than 0.99, indicating that the fitting accuracies are high.
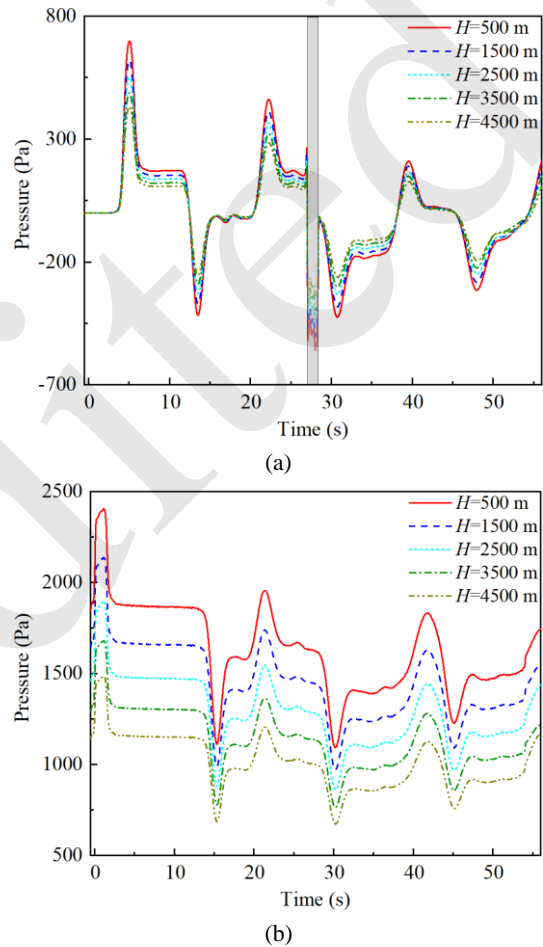

(a)

(b)

Fig. 15. Curves of pressure variation at observation points on the tunnel and train when trains pass through high-temperature tunnels at different altitudes: (a) TU_25; (b) TR_1
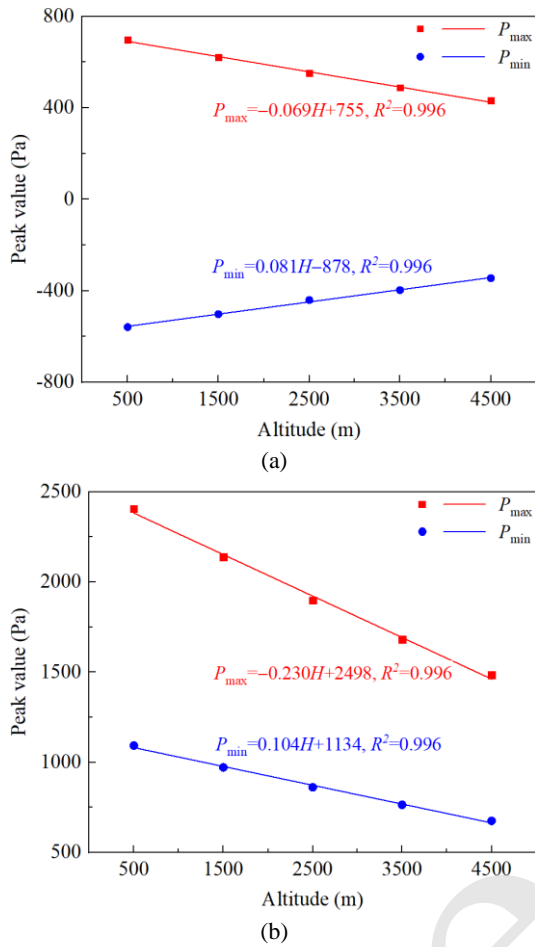
Fig. 16. Fitted curves between P_{max} and P_{min} of observation points on the tunnel and train and the altitude when trains pass through the high-temperature tunnel: (a) TU_25; (b) TR_1

4.2.2 Two trains passing each other in a tunnel

The pressure variation curves of TU_25 and TR_1 for two trains meeting in the high-temperature tunnels at different altitudes are shown in Fig. 17. The pressure waveforms remain unchanged, and the pressure peaks decrease with the rise in the altitude. The fitted curves and equations between the P_{max} and P_{min} of TU_25 and TR_1 and the altitude are shown in Fig. 18. The P_{max} and P_{min} decrease linearly with the rise in the altitude, and the fitted R^2 coefficients are more than 0.99. The rate of change in the P_{max} of TU_25 with the altitude of two trains passing by each other in a tunnel is much faster than that of a single train passing through a tunnel. As the P_{max} of TU_25 of two passing trains results from two compression waves provoked by the entries of the noses of the two trains, the effect of altitude on the P_{max} is greater. Fig.

S16 (Electronic Supplementary Materials) shows the pressure difference between TR_6a and TR_6b as the trains intersect in the high-temperature tunnels at different altitudes. The waveform of the variation curves remains unchanged, and as the decrease in the air density reduces the pressure of the region around the train, the peak-peak value decreases linearly with the rise in the altitude, and the fitted R^2 coefficient is more than 0.99.
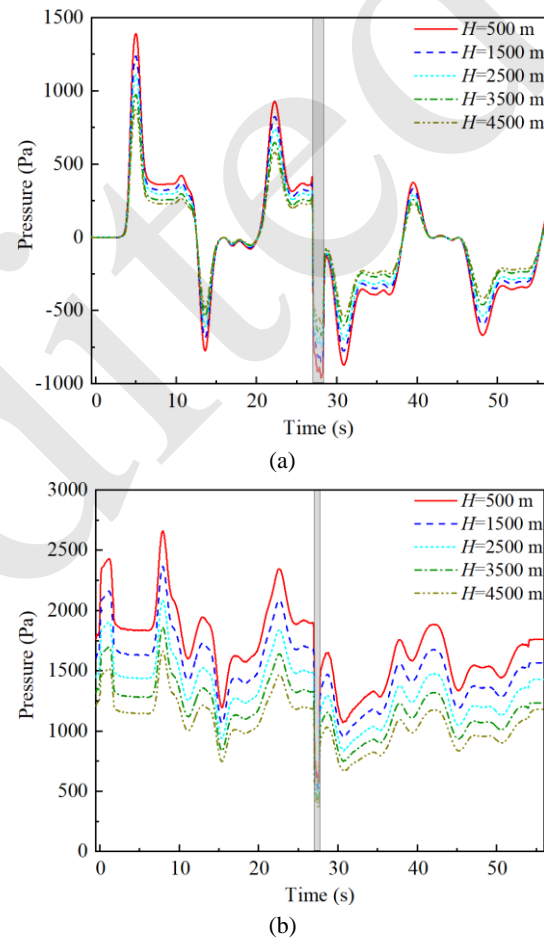

Fig. 17. Curves of pressure variation at observation points on the tunnel and train when two trains pass each other in high-temperature tunnels at different altitudes: (a) TU_25; (b) TR_1
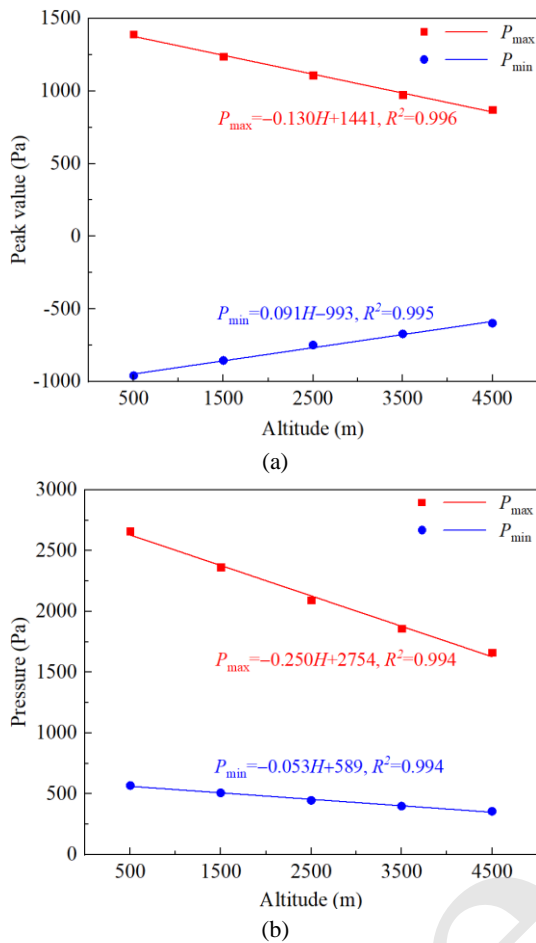
Fig. 18. Fitted curves between P_{max} and P_{min} at observation points and the altitude when two trains pass each other in high-temperature tunnels: (a) TU_25; (b) TR_1

5 Conclusions

In this study, considering the high temperature distribution along a tunnel in a high altitude area, the effects of high geotemperature and high altitude on pressure waves of trains passing through and passing by each other in a long tunnel were exa$_{min}$ed through numerical simulations. The results obtained can be summarized as follows: i) a representative tunnel length of 3 km was determined as an appropriate computational tunnel length for high-speed trains running in a long tunnel; ii) compared to the condition of a normal ambient-temperature tunnel, when trains go through a high geotemperature tunnel, the pressure peaks on the tunnel and train resulting from pressure waves decrease and appear increasingly earlier; iii) compared to the condition of the normal

ambient-temperature tunnel, when trains meet in a high geotemperature tunnel, the symmetrical point of the distribution of P_{max} along the tunnel moves slightly towards the tunnel entrance, and the distribution of P_{min} also changes; and iv) when trains cross and meet in the high-temperature tunnels at different altitudes, as the altitude rises, the waveforms of pressures on the tunnel and train and the pressure difference between two sides of the train remain unchanged, and the peaks decrease linearly. The results of this study show that when trains run in a long tunnel at high altitudes and high geotemperatures, the pressure amplitudes on the train surface and tunnel wall decrease integrally, and from an aerodynamic viewpoint, it is safer for the structure of the train body and tunnel. However, the changing temperature affects the location where the P_{max} and P_{min} appear on the tunnel wall. Thus, those locations may require more attention during tunnel design and maintenance, and should be more accurately located considering the changing temperature.

Author contributions

Lei Liu: methodology, investigation, software, data curation, writing – original draft. Lin Jing: conceptualization, funding acquisition, resources, supervision, writing – review & editing. Tian Li: writing – review & editing. Kaiyun Wang: methodology, writing – review & editing.

Conflict of interest

The authors declare that they have no known competing financial interests or personal relationships that could have appeared to influence the work reported in this paper.

References

Baker CJ, 2014. A review of train aerodynamics Part 1–Fundamentals. *The Aeronautical Journal*, 118(1201):201-228.
https://doi.org/10.1017/S000192400000909X

CEN European Standard, 2010. Railway Applications-Aerodynamics. Part 6: Requirements and Test Procedures for Cross Wind Assessment, CEN 14067–6:2010.

Chen MG, Mao J, Xi YH, 2023. Aerodynamic effect analysis of high-speed train entering and leaving single and double track tunnels under crosswind. *International Journal of*

Rail Transport, 1-23.
https://doi:10.1080/23248378.2023.2165182

Chen XD, Liu TH, Zhou XS, et al., 2017. Analysis of the aerodynamic effects of different nose lengths on two trains intersecting in a tunnel at 350 km/h. *Tunnelling and Underground Space Technology*, 66:77-90.
https://doi.org/10.1016/j.tust.2017.04.004

Chu CR, Chien SY, Wang CY, et al., 2014. Numerical simulation of two trains intersecting in a tunnel. *Tunnelling and Underground Space Technology*, 42:161-174.
http://dx.doi.org/10.1016/j.tust.2014.02.013

Gilbert T, Baker CJ, Quinn A, 2013a. Aerodynamic pressures around high-speed trains: the transition from unconfined to enclosed spaces. *Proceedings of the Institution of Mechanical Engineers, Part F: Journal of Rail and Rapid Transit*, 227(6):609-622.
https://doi.org/10.1177/0954409713494947

Gilbert T, Baker CJ, Quinn A, 2013b. Gusts caused by high-speed trains in confined spaces and tunnels. *Journal of Wind Engineering and Industrial Aerodynamics*, 121:39-48.
http://dx.doi.org/10.1016/j.jweia.2013.07.015

Huang J, He H, Yang WC, et al., 2022. Influence of altitude on transient pressure and ride comfort in railway tunnel. *Journal of Railway Science and Engineering*, 19(3):608-615 (in Chinese).
https://doi.org/10.19713/j.cnki.43-1423/u.T20210332

Ji P, Wang TT, Wu F, 2019. Calculation grid and turbulence model for numerical simulating pressure fluctuations in high-speed train tunnel. *Journal of Central South University*, 26: 2870−2877.
https://doi.org/10.1007/s11771-019-4220-6

Jing L, Liu K, Ren M, 2019. The transient response of car body and side windows for high-speed trains passing by each other in a tunnel. *Composites Part B*, 166:284-297.
https://doi.org/10.1016/j.compositesb.2018.11.144

Li T, Liang H, Zhang JY, et al., 2023. Numerical study on aerodynamic resistance reduction of high-speed train using vortex generator. *Engineering Applications of Computational Fluid Mechanics*, 17(1):e2153925.
https://doi-org-s.era.lib.swjtu.edu.cn:443/10.1080/19942060.2022.2153925

Li WH, Liu TH, Zhang J, et al., 2017. Aerodynamic study of two opposing moving trains in a tunnel based on different nose contours. *Journal of Applied Fluid Mechanics*, 10(5):1375-1386.
https://doi.org/10.18869/acadpub.jafm.73.242.27738

Li WH, Liu TH, Huo XS, et al., 2019. Influence of the enlarged portal length on pressure waves in railway tunnels with cross-section expansion. *Journal of Wind Engineering and Industrial Aerodynamics*, 190:10-22.
https://doi.org/10.1016/j.jweia.2019.03.031

Li WH, Liu TH, Chen ZW, et al., 2020. Comparative study on the unsteady slipstream induced by a single train and two trains passing each other in a tunnel. *Journal of Wind Engineering and Industrial Aerodynamics*, 198:104095.
https://doi.org/10.1016/j.jweia.2020.104095

Li WH, Liu TH, Martinez-Vazquez P, et al., 2021. Aerodynamic effects of a high-speed train travelling through adjoining & separated tunnels. *Tunnelling and Underground Space Technology*, 113:103973.
https://doi.org/10.1016/j.tust.2021.103973

Li WH, Liu TH, Martinez-Vazquez P, et al., 2022. Aerodynamic effects on a railway tunnel with partially changed cross-sectional area. *Journal of Central South University*, 29(8):2589–2604.
https://doi.org/10.1007/s11771-022-5113-7

Ling L, Hu YL, Yang ZJ, et al., 2022. Effect of Sichuan–Tibet Railway Special Meteorological Environment on Tunnel Aerodynamic Drag of Electric Multiple Unit Train. *Journal of Southwest Jiaotong University*, 57(1):158-165 (in Chinese).
https://doi.org/10.3969/j.issn.0258-2724.20190998

Liu F, Yao S, Zhang J, et al.,2018. Field measurements of aerodynamic pressures in high-speed railway tunnels. *Tunnelling and Underground Space Technology*, 72:97-106.
https://doi.org/10.1016/j.jweia.2011.10.008

Liu K, Jing L, Ren M, 2018. The characteristics of air wave induced by two high-speed trains passing by each other in a tunnel. *Advances in Mechanical Engineering*, 10(3):1-16.
https://doi:10.1177/1687814018766970

Liu TH, Chen XD, Li WH, et al., 2017a. Field study on the interior pressure variations in high-speed trains passing through tunnels of different lengths. *Journal of Wind Engineering and Industrial Aerodynamics*, 169:54-66.
http://dx.doi.org/10.1016/j.jweia.2017.07.004

Liu TH, Chen ZW, Chen XD, et al., 2017b. Transient loads and their influence on the dynamic responses of trains in a tunnel. *Tunnelling and Underground Space Technology*, 66:121-133.
http://dx.doi.org/10.1016/j.tust.2017.04.009

Liu TH, Chen ZW, Zhou XS, et al., 2018. A CFD analysis of the aerodynamics of a high-speed train passing through a windbreak transition under crosswind. *Engineering Applications of Computational Fluid Mechanics*, 12(1):137-151.
http://dx.doi.org/10.1080/19942060.2017.1360211

Luo JJ, 2016. Aerodynamic effect induced by high-speed train entering into tunnel in high altitude area. *Journal of Southwest Jiaotong University*, 51(4):607-614 (in Chinese).
https://doi.org/10.3969/j.issn.0258-2724.201.04.002

Miyachi T, Iida M, Fukuda T, et al., 2016. Nondimensional maximum pressure gradient of tunnel compression waves generated by offset running axisymmetric trains. *Journal of Wind Engineering and Industrial Aerodynamics*, 157:23-35.
http://dx.doi.org/10.1016/j.jweia.2016.07.015

Niu JQ, Zhou D, Liu TH, et al., 2017. Numerical simulation of aerodynamic performance of a couple multiple units high-speed train. *Vehicle System Dynamics*, 55(5):681-703.

https://doi.org/10.1080/00423114.2016.1277769

Niu JQ, Zhou D, Liu F, et al., 2018a. Effect of train length on fluctuating aerodynamic pressure wave in tunnels and method for determining the amplitude of pressure wave on trains. *Tunnelling and Underground Space Technology*, 80:277-289.
https://doi.org/10.1016/j.tust.2018.07.031

Niu JQ, Zhou D, Wang YM, 2018b. Numerical comparison of aerodynamic performance of stationary and moving trains with or without windbreak wall under crosswind. *Journal of Wind Engineering and Industrial Aerodynamics.*, 182:1-15.
https://doi.org/10.1016/j.jweia.2018.09.011

Raghunathan RS, Kim HD, Setoguchi T, 2002. Aerodynamics of high-speed railway train. *Progress In Aerospace Sciences*, 38(6-7):469-514.
https://doi.org/10.1016/S0376-0421(02)00029-5

Wang JY, Wang TT, Yang MZ, et al., 2021. Effect of localized high temperature on the aerodynamic performance of a high-speed train passing through a tunnel. *Journal of Wind Engineering and Industrial Aerodynamics*, 208:104444.
https://doi.org/10.1016/j.jweia.2020.104444

Wang JY, Wang TT, Zhang L, et al., 2022. Research on the characteristics of micro-pressure waves in high-temperature geothermal railway tunnels and a self-satisfying mitigation method. *Journal of Wind Engineering and Industrial Aerodynamics*, 225:104998.
https://doi.org/10.1016/j.jweia.2022.104998

Wang TT, Wu F, Yang MZ, et al., 2018. Reduction of pressure transients of high-speed train passing through a tunnel by cross-section increase. *Journal of Wind Engineering and Industrial Aerodynamics*, 183:235-242.
https://doi.org/10.1016/j.jweia.2018.11.001

Xue RD, Xiong XH, Wang KW, et al., 2023. Influence of variable cross-section on pressure transients and unsteady slipstream in a long tunnel when high-speed train passes through. *Journal of Central South University*, 30(4):1027–1046.
https://doi.org/10.1007/s11771-023-5273-0

Yang WC, Deng E, Lei MF, et al., 2019. Transient aerodynamic performance of high-speed trains when passing through two windproof facilities under crosswinds: A comparative study. *Engineering Structure*, 188:729-744.
https://doi.org/10.1016/j.engstruct.2019.03.070

Zarnaghsh A, Abouali O, Emdad H, et al., 2019. A numerical study of the train-induced unsteady airflow in a tunnel and its effects on the performance of jet fans. *Journal of Wind Engineering and Industrial Aerodynamics*, 187:1-14.
https://doi.org/10.1016/j.jweia.2019.01.012

Zhang DL, Sun ZY, Fang Q, 2022. Scientific problems and research proposals for Sichuan–Tibet railway tunnel construction. *Underground Space*, 7(3):419-439.
https://doi.org/10.1016/j.undsp.2021.10.002

Zhang J, 2021. Research on distribution characteristics of geothermal field and thermal hazard prevention measures in Layue tunnel. MaS Thesis, Southwest Jiaotong University, Chengdu, China (in Chinese).

Zhang L, Li T, Zhang J, 2021. Research on aerodynamic shape optimization of trains with different dimensional design variables. *International Journal of Rail Transportation*, 9(5):479-501.
https://doi.org/10.1080/23248378.2020.1817803

Zhang L, Thurow K, Stoll N, et al., 2018. Influence of the geometry of equal-transect oblique tunnel portal on compression wave and micro-pressure wave generated by high-speed trains entering tunnels. *Journal of Wind Engineering and Industrial Aerodynamics*, 178:1-17.
https://doi.org/10.1016/j.jweia.2018.05.003

Zhao KM, Yuan YP, Jiang FJ, et al., 2023. Numerical investigation on temperature–humidity field under mechanical ventilation in the construction period of hot-humid tunnel along the Sichuan–Tibet Railway. *Underground Space*, 8:123-143.
https://doi.org/10.1016/j.undsp.2022.04.004

Zhou MM, Liu TH, Xia YT, et al., 2022. Comparative investigations of pressure waves induced by trains passing through a tunnel with different speed modes. *Journal of Central South University*, 29(8):2639–2653.
https://doi.org/10.1007/s11771-022-5098-2

Electronic supplementary materials
Figs. S1–S16; Table S1.

中文概要

题 目：高地温和高海拔对高速列车长大隧道运行压力波的影响

作 者：刘磊，敬霖✉，李田，王开云

机 构：西南交通大学，轨道交通运载系统全国重点实验室，中国成都，610031

目 的：高速列车隧道运行时产生的空气压力波会对车体及隧道结构的安全造成不良影响，是铁路隧道设计中需要解决的关键科技问题之一。高海拔地区高速铁路隧道具有长度大的显著特点，并且低气压、高地热等特殊线路环境条件将会对隧道内空气的密度、粘度等参数产生影响，从而影响列车隧道运行时产生的空气压力波的特性。研究高地温和高海拔对高速列车长大隧道运行压力波的影响，对于保证隧道高速列车在该地区隧道内运行时车体及隧道的结构安全重要价值，并可为隧道的设计提供技术支持。

创新点：1.通过分析隧道长度对于高速列车隧道运行压力

波特性的影响，确定了具有代表性的隧道长度用于仿真模拟，以降低计算成本和有效反映高速列车长大隧道运行压力波特性。2.建立的计算空气动力学仿真模型中考虑了高温沿整个隧道的分布情况，以模拟更加真实的高地温环境。

方　法：采用采用三维、非定常、可压缩雷诺时均方程和RNG $k\!-\!\varepsilon$ 湍流模型，研究高地温和高海拔对高速列车隧道通过和隧道交会压力波特性的影响。

结　论：1.与正常环境温度的情况相比，当高速列车通过高地温隧道时，隧道和列车表面的压力峰值减小，并且出现得越来越早；2.与正常环境温度的情况相比，当高速列车在高地温隧道中交会时，$P_{\max}$ 沿隧道分布的对称点向隧道入口移动，$P_{\min}$ 的分布也发生了变化；3.随着海拔的上升，列车隧道通过及交会时，隧道和列车表面的压力波形以及列车两侧的压差保持不变，并且峰值线性减小；4.列车在高海拔、高地温的长大隧道中运行时，列车和隧道表面的压力幅值整体减小；然而，温度的变化会影响隧道表面压力幅值出现的位置，在隧道设计和维护时，这些位置可能需要更多的关注，并且更准确地进行定位。

关键词：高地温；高海拔；高速列车；长大隧道；压力波